

# Birefringence measurements in human skin using polarization-sensitive optical coherence tomography

Mark C. Pierce  
John Strasswimmer  
B. Hyle Park  
Barry Cense  
Johannes F. de Boer  
Harvard Medical School  
Massachusetts General Hospital  
Wellman Center for Photomedicine  
50 Blossom Street  
Boston, Massachusetts 02114

**Abstract.** Optical coherence tomography enables cross-sectional imaging of tissue structure to depths of around 1.5 mm, at high-resolution and in real time. Incorporation of polarization sensitivity (PS) provides an additional contrast mechanism which is complementary to images mapping backscattered intensity only. We present here polarization-sensitive optical coherence tomography (OCT) images of human skin *in vivo*, demonstrating the ability of the technique to visualize and quantify the birefringent properties of skin. Variation in normal skin birefringence according to anatomical location is demonstrated, and discussed in relation to collagen distribution at each location. From measurements on a sample of five human volunteers, mean double-pass phase retardation rates of  $0.340 \pm 0.143$ ,  $0.250 \pm 0.076$ , and  $0.592 \pm 0.142$  deg/ $\mu\text{m}$  were obtained for the dorsal hand, temple, and lower back regions, respectively. We demonstrate how averaging the Stokes parameters of backscattered light over a range of axial and lateral dimensions results in a reduction of speckle-induced noise. Examples of PS-OCT images from skin sites following wound healing and repair are also presented and discussed. © 2004 Society of Photo-Optical Instrumentation Engineers. [DOI: 10.1117/1.1645797]

Keywords: optical imaging; polarization; Stokes parameters; dermatology; collagen; wound healing.

Paper 014013 received Apr. 14, 2003; revised manuscript received Jul. 1, 2003; accepted for publication Jul. 1, 2003.

## 1 Introduction

Optical coherence tomography (OCT) is a recently developed technique that permits noninvasive, cross-sectional imaging of subsurface tissue structure.<sup>1</sup> Conventional OCT images are oriented analogously to a vertical section in histology, with a typical resolution of around 10  $\mu\text{m}$  achievable to depths of 1.5–2 mm in tissue. Advances in optical source development,<sup>2–4</sup> data acquisition, and imaging speed<sup>5,6</sup> and the development of probes tailored to enable access to particular organs<sup>7,8</sup> has resulted in the application of OCT across a range of clinical areas.<sup>9</sup> Previously reported investigations of OCT in dermatology have demonstrated the ability of the technique to delineate epidermal and dermal layers, identify appendages including eccrine ducts and pilosebaceous units, and observation of conditions including inflammation and blistering.<sup>10–16</sup>

Significant enhancements to OCT technology have since been realized, including improvement in resolution, imaging depths that extend beyond 1 mm, and considerably reduced imaging times. Incorporation of polarization sensitivity<sup>17–19</sup> enables the polarization state of light to be detected and quantified, which is particularly significant when birefringent tissues are of interest. Many types of tissue exhibit intrinsic and/or form birefringence, especially those with a significant collagen content, including tendon, ligament, and skin. The collagen content of the skin is particularly important, since combined with elastin in the dermis, it provides the extracel-

lular matrix upon which the impermeable epidermal layer is grown. Loss of collagen structure and integrity is frequently associated with abnormalities of the skin, including skin cancer and thermal injury, suggesting that birefringence measurements may prove valuable as a diagnostic indicator of certain dermatologic pathologies.

Polarization-sensitive optical coherence tomography (PS-OCT) was originally implemented by the addition of bulk polarization optics to conventional OCT systems, with interference fringes formed by light in orthogonal polarization states detected separately. Polarization-related phenomena have been observed using single-detector systems, although without the employment of true polarization diversity detection, such measurements remain qualitative and susceptible to error and misinterpretation. A complete description of polarization effects in OCT requires use of the Stokes vector<sup>20</sup> or Mueller matrix formalisms. Sixteen-element Mueller matrices have been determined for *in vitro* biological samples using bulk-optic PS-OCT systems,<sup>21–23</sup> although for successful deployment of PS-OCT in the clinical setting, high-speed fiber-based systems were developed, thereby reducing sensitivity to misalignment,<sup>24</sup> with imaging at 2048 A lines per second recently reported.<sup>6,25</sup>

## 2 Materials and Methods

The design and implementation of our PS-OCT system are described elsewhere.<sup>25</sup> Briefly, a semiconductor optical amplifier light source with a center wavelength of 1310 nm and full

Address all correspondence to Mark C. Pierce. Tel: 617-724-5532; Fax: 617-726-4103; E-mail: pierce@helix.mgh.harvard.edu

width at half maximum (FWHM) bandwidth of 70 nm is coupled via optical fiber to an electro-optic polarization modulator. After transmission through the modulator and a fiber optic circulator, a fiber optic splitter divides light in a 90:10 ratio between the sample and reference arms, respectively. Use of a circulator and an uneven splitting ratio increases the power efficiency of the system relative to designs based on a standard 50:50 split Michelson configuration.<sup>26,27</sup> A rapid scanning optical delay line is used for reference path scanning at 2048 A lines per second, permitting real-time data acquisition. Light is directed onto the skin via a light, compact handheld probe, resulting in an incident power of 7 mW at the tissue, focused on a spot of around 20  $\mu\text{m}$  diameter. This power level is below the safe occupational exposure level established by the American National Standards Institute (ANSI Z136.1). Light reflected from the skin is recombined with light from the reference mirror and coupled via the optical circulator to an all-fiber optic polarizing beamsplitter, with orthogonal polarization states each detected by fiber-pigtailed photodiodes. Signals at each of the two detectors are amplified, filtered, and digitized before all subsequent data processing and display are performed in software.

Extraction of the sine and cosine components of the full interference fringe patterns at each detector enables the Stokes parameters of backscattered light to be calculated as a function of depth within the sample. Conventional OCT intensity images are formed by displaying the Stokes parameter  $I(z)$  on a logarithmic gray scale, with black representing strong backscattering intensity. To obtain polarization-sensitive images, light incident on the tissue sample is modulated between two independent polarization states, orthogonal in the Poincaré sphere, for alternate A lines. Use of these two different states maximizes the accuracy of the polarization information obtained, and ensures that tissue birefringence will be detected regardless of the material's optic axis orientation. For each pair of A lines, the polarization states of light incident at the sample surface are described by the Stokes vectors  $[Q(0), U(0), V(0)]_{1,2}$ . Upon propagation within tissue, these polarization states may change due to effects including scattering, birefringence, and dichroism, and are described at a depth  $z$  within the sample by Stokes vectors  $[Q(z), U(z), V(z)]_{1,2}$ . In the Poincaré sphere, these changes in the polarization state of light are described by rotation of the Stokes vectors through a retardation angle  $\theta$ , which in the case of pure birefringence, is about an axis lying in the  $QU$  plane. In addition to tissue birefringence, in a fiber-based PS-OCT system, the polarization state may also change as a result of fiber birefringence, meaning that rotation of the Stokes vectors is no longer constrained about an axis in the  $QU$  plane. We account for the contribution of fiber birefringence by determining the orientation of a unique optic axis as a function of depth within tissue, and the angle through which our pair of Stokes vectors is rotated about this axis.<sup>6,28</sup> By determining the phase retardation angle relative to the tissue surface state for each A line, we are insensitive to changes in the polarization state of light which may be induced by either static or dynamic changes in sample arm fiber birefringence on time scales longer than that taken to acquire each A line, which for the system described here is 500  $\mu\text{s}$ . Each polarization-sensitive image thus comprises 1024 lines, with phase retardation angles displayed on a gray scale that cycles

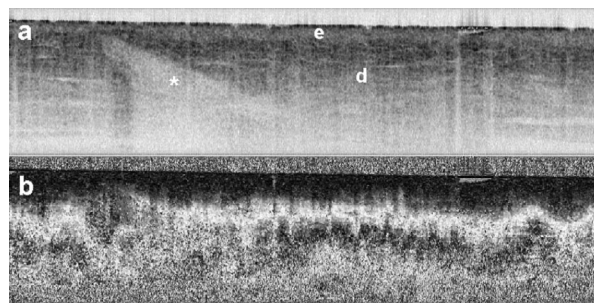


**Fig. 1** Conventional (a) and polarization-sensitive (b) images of skin at the lower back of a human volunteer. The images are 5 mm wide  $\times$  1.2 mm in physical depth ( $n=1.4$ ). e—Epidermis; d—dermis; \*—hair follicle.

from black ( $0^\circ$ ) to white ( $180^\circ$ ) and returns to black at  $360^\circ$ .

All experiments were performed on healthy volunteers, recruited under a protocol approved by the Institutional Review Board of Massachusetts General Hospital. Each set of OCT images (both intensity and polarization-sensitive images) was acquired, processed, and displayed in 1 s. All images presented here are 5 mm wide and 1.2 mm in physical depth, using the approximation of a constant tissue refractive index of 1.4. Images are displayed on a logarithmic gray scale over a 55 dB dynamic range.

### 3 Results

Representative conventional and polarization-sensitive images of skin at the lower back and temple regions are shown in Figs. 1 and 2, respectively. The layered structure of skin comprising epidermal, e, and dermal, d, layers is evident in both conventional images. Features including a hair follicle (\*) are observed in the skin of the lower back, which also exhibits a thicker epidermal layer compared to the skin of the temple. A greater density of sebaceous glands in skin of the facial region leads to a less structured appearance within the papillary dermis compared to the lower back, where a strongly backscattering, fibrous layer is observed. Further differences in the properties of skin at these two locations are revealed by the corresponding polarization-sensitive images [Figs. 1(b) and 2(b)]. At both locations, there is minimal change in the polarization state of light within the epidermal layer, as indicated by the image remaining black within this region. However, birefringence within the dermal layers at these skin sites ap-

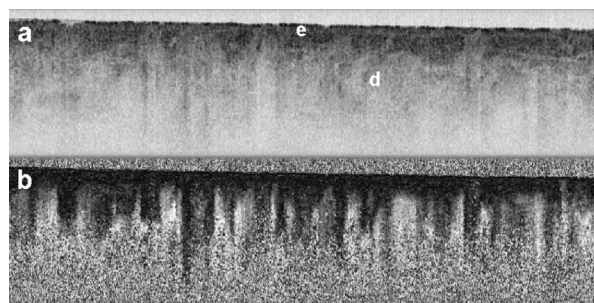


**Fig. 2** Conventional (a) and polarization-sensitive (b) images of skin at the temple of a human volunteer. The images are 5 mm wide  $\times$  1.2 mm in physical depth ( $n=1.4$ ). e—Epidermis; d—dermis.

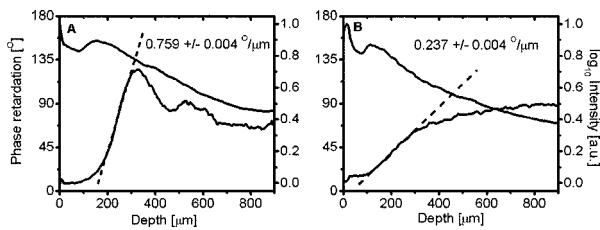


**Fig. 3** Mean phase retardation and intensity as a function of depth for the images of the lower back (a) and temple (b) shown in Figs. 1 and 2, respectively. The gradient of a linear least-squares fit to the phase retardation data is shown in each case, along with the associated fitting error.

appears visibly different, as indicated by the contrast of the transition from black to white in each image. Skin of the lower back [Fig. 1(b)] demonstrates changes in the polarization state of light within the dermal layer, with the measured phase retardation angle cycling over  $360^\circ$  (black to white to black). In contrast, the lack of strong banding observed in Fig. 2(b), corresponding to skin of the temple, indicates considerably lower birefringence at this location.

The information contained within these polarization-sensitive images can be displayed quantitatively by calculating the mean phase retardation angle as a function of depth over the full width of an image. Figures 3(a) and 3(b) show both the mean intensity and phase retardation corresponding to Figs. 1 and 2. The depth of the secondary peak in the intensity plots indicates the location of the epidermal–dermal boundary, measured at  $117 \pm 10 \mu\text{m}$  for the temple and  $155 \pm 10 \mu\text{m}$  at the lower back. The phase retardation graphs for both skin locations demonstrate minimal change in the polarization state of light within this epidermal layer, before the accumulated phase retardation increases as light propagates within the dermis. Applying a least-squares fit to the linear portion of these phase retardation plots enables skin birefringence to be quantified in terms of the (double-pass) phase retardation rate and associated fitting error, with values of  $0.759 \pm 0.004$  and  $0.237 \pm 0.004 \text{ deg}/\mu\text{m}$  measured for the lower back and temple locations shown in Figs. 1 and 2, respectively. The observed offset at the tissue surface is due to variance in the computed Stokes parameters that arises from speckle. This noise can be reduced by averaging the Stokes parameters over distances larger than the coherence length of the source.<sup>29</sup> Figure 4 demonstrates how the phase offset observed in Fig. 3(a) is reduced by averaging the Stokes parameters over different spatial scales in both axial and lateral directions. Stokes parameters were averaged over  $160 \mu\text{m}$  in the lateral direction and  $14.1 \mu\text{m}$  in depth for the graphs presented in Fig. 3.

Figures 1(b) and 2(b) demonstrate how tissue birefringence can vary within an image: some regions indicate retardation values around  $180^\circ$  (white) while in neighboring regions the retardation remains low (dark gray). The intention of this study was to examine anatomical variations in skin birefringence rather than small-scale local variations. Therefore, to assign a single retardation value to the region of tissue imaged, we determined phase retardation values averaged over the full width of each image. To evaluate the reproducibility of our observations, birefringence measurements were taken

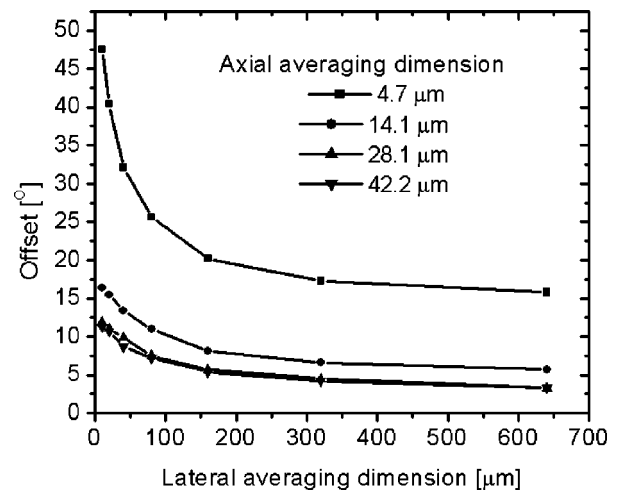


**Fig. 4** Reduction in phase offset for the data displayed in Fig. 3(a), as a function of the axial and lateral dimensions over which the Stokes parameters are averaged.

at the lower back, temple, and back of the right hand, of a group of five healthy male volunteers, aged between 24 and 35 years. For each volunteer, 15 PS-OCT images were taken at each location, consisting of 3 neighboring groups of 5 scans. Each scan was 5 mm wide with successive scans 1 mm apart, such that each group covered a  $5 \times 5 \text{ mm}^2$  area. Least-squares fits were applied to each phase retardation plot as demonstrated previously, yielding 15 values of phase retardation rate ( $\text{deg}/\mu\text{m}$ ) with associated individual fitting errors for each location. Mean phase retardation rates were then calculated for the lower back, temple, and hand for each volunteer. The results of these measurements are shown in Fig. 5, with accompanying error bars indicating the standard error on the mean. The measured phase retardation rates exhibit variation according to the skin location, with the temple region exhibiting the lowest value for all subjects. Conversely, skin of the lower back provided the highest value for all subjects, with

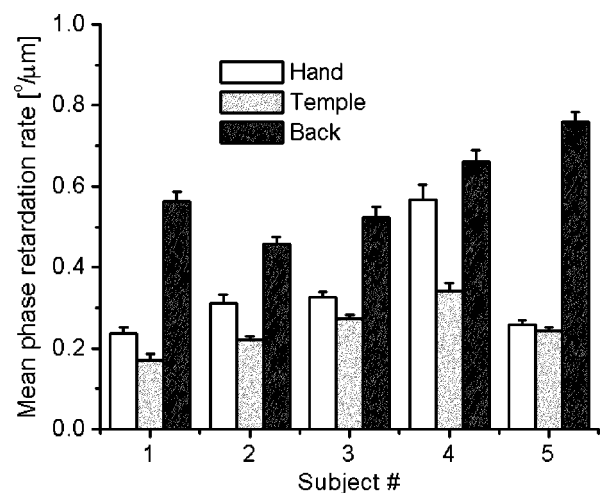


**Fig. 5** Bar graph of the mean phase retardation rate with standard error on the mean ( $\text{deg}/\mu\text{m}$ ) for the hand, temple, and lower back of each of five volunteers. Each data point was obtained from 15 separate measurements at each location.

**Table 1** Mean (double-pass) phase retardation rate, standard deviation, and standard error on the mean for the hand, temple, and lower back regions, determined from all data samples. ( $n$ =five volunteers $\times$ 15 scans at each location=75 measurements per location.)

	Mean phase retardation (deg/ $\mu$ m)	Standard deviation (deg/ $\mu$ m)	Standard error on mean (deg/ $\mu$ m)
Hand ( $n=75$ )	0.340	0.143	0.017
Temple ( $n=75$ )	0.250	0.076	0.009
Lower back ( $n=75$ )	0.592	0.142	0.016

skin of the hand yielding intermediate values. Table 1 provides the mean phase retardation rate, standard deviation, and standard error on the mean for data combined from all volunteers, at each of the three locations investigated.

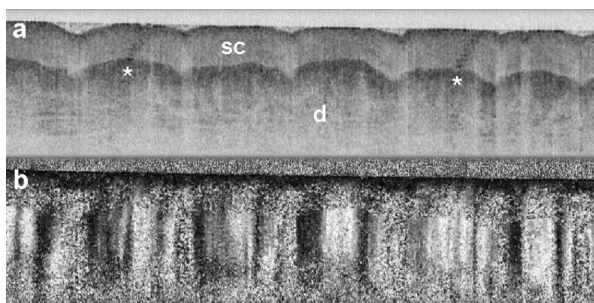
To further illustrate the intrinsic variation of skin birefringence with anatomical location, Fig. 6 presents PS-OCT images at the index fingertip of a volunteer. Ridges that form the fingerprint unique to this volunteer are immediately evident in the conventional OCT image, with eccrine ducts extending to the skin surface through the characteristically thick stratum corneum (sc) common to acral skin of the hands and feet. The horizontal black–white banding observed in earlier polarization-sensitive images of skin on the lower back and temple [Figs. 1(b) and 2(b)], is replaced by three distinct regimes of polarization behavior. Upon propagation through the stratum corneum, the polarization state of light varies randomly, and is apparent from the random phase retardation angles mapped between black and white within this region. Upon entering the papillary dermis, light is seen to remain in some arbitrary polarization state, with a degree of correlation apparent over spatial scales on the order of 200  $\mu$ m. Within the lower dermis, depolarization due to multiple scattering dominates and the polarization-sensitive image again becomes randomized. One possible explanation for randomization of the polarization state of light observed in the stratum corneum is that the flattened, keratinized cells present within this layer each act as individual wave plates with random retardation, although this hypothesis requires further investigation.

Figure 7 demonstrates the effect of wound healing on skin birefringence; this image was acquired at the site of mature scar tissue on the arm of a volunteer. The image traverses the

boundary between normal skin (left) and scar tissue (right), with the scar region providing a slightly stronger (darker) backscattering signal compared to the normal region in Fig. 7(a). Examination of the corresponding polarization-sensitive image reveals multiple black–white bands within the scar region that are absent in the normal (left) side of the image. The appearance of strong multiple banding within both young and old scar tissue has been observed consistently during imaging of scar sites on the skin, which we attribute to the presence of newly formed collagen at these locations, which exhibit increased birefringence.

#### 4 Discussion

The polarization properties of the skin provide a contrast mechanism in addition to backscattered light intensity which may be exploited when observing or imaging the skin. PS-OCT enables changes in the polarization state of light to be visualized and quantified in a depth-resolved manner, both at single points in time and over extended courses of time. We have observed the ability of components of the skin to alter the polarization state of light, and attribute this to the birefringent nature of collagen fibers, which along with elastin fibers, provides the dermal layer with mechanical strength and organization. While the presence of collagen is common to skin at all locations on the body, the size, distribution, and relative concentration of individual fibers are known to vary according to the location. Our observations of variable birefringence with location reported here may be understood by consideration of the known collagen distribution at the locations examined. The relatively thick skin of the torso and limbs has a



**Fig. 6** Conventional (a) and polarization-sensitive (b) images of skin at the index fingertip of a human volunteer. The images are 5 mm wide  $\times$  1.2 mm in physical depth ( $n=1.4$ ). sc—Stratum corneum; d—dermis; \*—eccrine ducts.

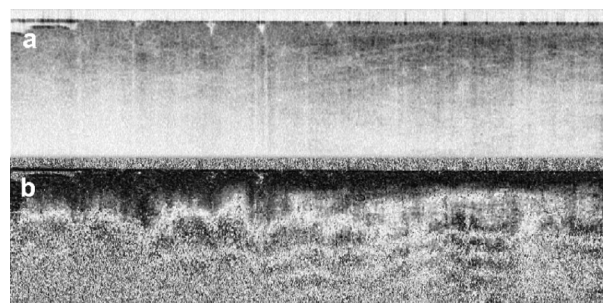


**Fig. 7** Conventional (a) and polarization-sensitive (b) images of skin at the site of scar tissue on the arm of a human volunteer. The images are 5 mm wide  $\times$  1.2 mm in physical depth ( $n=1.4$ ). To the left side of the image is normal skin, to the right is mature scar tissue.

thick dermal layer, made up of large bundles of collagen fibers, which we expect to exhibit significant birefringence. Thinner skin covering the face comprises a network of finer collagen bundles, combined with a particularly high density of eccrine glands, resulting in lower birefringence. Collagen remodeling and repair are known to be a fundamental aspect of the wound healing process, and, as we have seen, skin in regions of scar tissue is particularly birefringent.

Collagen birefringence has been previously reported,<sup>30,31</sup> as have dynamic changes in birefringence due to thermal denaturation,<sup>31,32</sup> although other potentially influential factors including age, photodamage, and wound healing response have been poorly categorized *in vivo*. As we have demonstrated here, variation with anatomical location can be significant, although the measurements appear to be consistent across a limited set of samples.

## 5 Conclusions

PS-OCT provides noninvasive imaging and quantification of both the skin structure and polarization properties in real time. We anticipate that birefringence measurements in human skin may prove useful as an indicator of collagen integrity, which itself is related to a wide range of dermatological conditions.

## Acknowledgments

Research grants from the Whitaker Foundation (Grant No. 26083) and Department of Defense (Grant No. F4 9620-01-1-0014) are gratefully acknowledged.

## References

- D. Huang, E. A. Swanson, C. P. Lin, J. S. Schuman, W. G. Stinson, W. Chang, M. R. Hee, T. Flotte, K. Gregory, C. A. Puliafito, and J. G. Fujimoto, "Optical coherence tomography," *Science* **254**, 1178–1181 (1991).
- B. E. Bouma, G. J. Tearney, I. P. Bilinsky, B. Golubovic, and J. G. Fujimoto, "Self-phase-modulated Kerr-lens mode-locked Cr:forsterite laser source for optical coherence tomography," *Opt. Lett.* **21**, 1839–1841 (1996).
- W. Drexler, U. Morgner, F. X. Kärtner, C. Pitris, S. A. Boppart, X. D. Li, E. P. Ippen, and J. G. Fujimoto, "*In vivo* ultrahigh-resolution optical coherence tomography," *Opt. Lett.* **24**, 1221–1223 (1999).
- I. Hartl, X. D. Li, C. Chudoba, R. K. Ghanta, T. H. Ko, and J. G. Fujimoto, "Ultrahigh-resolution optical coherence tomography using continuum generation in an air-silica microstructured optical fiber," *Opt. Lett.* **26**, 608–610 (2001).
- A. M. Rollins, M. D. Kulkarni, S. Yazdanfar, R. Ung-arunyawee, and J. A. Izatt, "*In vivo* video rate optical coherence tomography," *Opt. Express* **3**, 219–229 (1998).
- B. H. Park, M. C. Pierce, B. Cense, and J. F. de Boer, "Real-time multi-functional optical coherence tomography," *Opt. Express* **11**, 782–793 (2003).
- G. J. Tearney, M. E. Brezinski, B. E. Bouma, S. A. Boppart, C. Pitris, J. F. Southern, and J. G. Fujimoto, "*In vivo* endoscopic biopsy with optical coherence tomography," *Science* **276**, 2037–2039 (1997).
- X. Li, C. Chudoba, T. Ko, C. Pitris, and J. G. Fujimoto, "Imaging needle for optical coherence tomography," *Opt. Lett.* **25**, 1520–1522 (2000).
- Handbook of Optical Coherence Tomography*, B. E. Bouma and G. J. Tearney, Eds., Dekker, New York (2002).
- J. M. Schmitt, M. J. Yadlowsky, and R. F. Bonner, "Subsurface imaging of living skin with optical coherence microscopy," *Dermatology (Basel, Switz.)* **191**, 93–98 (1995).
- J. Welzel, E. Lankenau, R. Birngruber, and R. Engelhardt, "Optical coherence tomography of the human skin," *J. Am. Acad. Dermatol.* **37**, 958–963 (1997).
- Y. Pan and D. L. Farkas, "Noninvasive imaging of living human skin with dual-wavelength optical coherence tomography in two and three dimensions," *J. Biomed. Opt.* **3**, 446–455 (1998).
- A. Knüttel and M. Boehlau-Godau, "Spatially confined and temporally resolved refractive index and scattering evaluation in human skin performed with optical coherence tomography," *J. Biomed. Opt.* **5**, 83–92 (2000).
- A. G. Podoleanu, J. A. Rogers, and D. A. Jackson, "Three-dimensional OCT images from retina and skin," *Opt. Express* **7**, 292–298 (2000).
- N. D. Gladkova, G. A. Petrova, N. K. Nikulin, S. G. Radenska-Lopovok, L. B. Snopova, Y. P. Chumakov, V. A. Nasonova, V. M. Gelikonov, G. V. Gelikonov, R. V. Kuranov, A. M. Sergeev, and F. I. Feldchtein, "*In vivo* optical coherence tomography imaging of human skin: Norm and pathology," *Skin Res. Tech.* **6**, 6–16 (2000).
- J. Welzel, "Optical coherence tomography in dermatology: A review," *Skin Res. Tech.* **7**, 1–9 (2001).
- M. R. Hee, D. Huang, E. A. Swanson, and J. G. Fujimoto, "Polarization-sensitive low-coherence reflectometer for birefringence characterization and ranging," *J. Opt. Soc. Am. A* **9**, 903–908 (1992).
- J. F. de Boer, T. E. Milner, M. J. C. van Gemert, and J. S. Nelson, "Two-dimensional birefringence imaging in biological tissue by polarization-sensitive optical coherence tomography," *Opt. Lett.* **22**, 934–936 (1997).
- M. J. Everett, K. Schoenenberger, B. W. Colston, Jr., and L. B. Da Silva, "Birefringence characterization of biological tissue by use of optical coherence tomography," *Opt. Lett.* **23**, 228–230 (1998).
- J. F. de Boer, T. E. Milner, and J. S. Nelson, "Determination of the depth-resolved Stokes parameters of light backscattered from turbid media by use of polarization-sensitive optical coherence tomography," *Opt. Lett.* **24**, 300–302 (1999).
- G. Yao and L. V. Wang, "Two-dimensional depth-resolved Mueller matrix characterization of biological tissue by optical coherence tomography," *Opt. Lett.* **24**, 537–539 (1999).
- S. Jiao and L. V. Wang, "Two-dimensional depth-resolved Mueller matrix of biological tissue measured with double-beam polarization-sensitive optical coherence tomography," *Opt. Lett.* **27**, 101–103 (2002).
- Y. Yasuno, S. Makita, Y. Sutoh, M. Itoh, and T. Yatagai, "Birefringence imaging of human skin by polarization-sensitive spectral interferometric optical coherence tomography," *Opt. Lett.* **27**, 1803–1805 (2002).
- C. E. Saxer, J. F. de Boer, B. H. Park, Y. H. Zhao, Z. P. Chen, and J. S. Nelson, "High-speed fiber-based polarization-sensitive optical coherence tomography of *in vivo* human skin," *Opt. Lett.* **25**, 1355–1357 (2000).
- M. C. Pierce, B. H. Park, B. Cense, and J. F. de Boer, "Simultaneous intensity, birefringence, and flow measurements with high-speed fiber-based optical coherence tomography," *Opt. Lett.* **27**, 1534–1536 (2002).
- B. E. Bouma and G. J. Tearney, "Power-efficient nonreciprocal interferometer and linear-scanning fiber-optic catheter for optical coherence tomography," *Opt. Lett.* **24**, 531–533 (1999).
- A. M. Rollins and J. A. Izatt, "Optimal interferometer designs for optical coherence tomography," *Opt. Lett.* **24**, 1484–1486 (1999).
- B. H. Park, C. Saxer, S. M. Srinivas, J. S. Nelson, and J. F. de Boer, "*In vivo* burn depth determination by high-speed fiber-based polarization sensitive optical coherence tomography," *J. Biomed. Opt.* **6**, 474–479 (2001).
- J. F. de Boer and T. E. Milner, "Review of polarization sensitive optical coherence tomography and Stokes vector determination," *J. Biomed. Opt.* **7**, 359–371 (2002).
- S. Thomsen, "Pathological analysis of photothermal and photomechanical effects of laser-tissue interactions," *Photochem. Photobiol.* **53**, 825–835 (1991).
- D. J. Maitland and J. T. Walsh, "Quantitative measurements of linear birefringence during heating of native collagen," *Lasers Surg. Med.* **20**, 310–318 (1997).
- J. F. de Boer, S. M. Srinivas, A. Malekafzali, Z. P. Chen, and J. S. Nelson, "Imaging thermally damaged tissue by polarization sensitive optical coherence tomography," *Opt. Express* **3**, 212–218 (1998).